PASJ: Publ. Astron. Soc. Japan **63**, S991–S1007, 2011 November 25

Suzaku Observations of Iron K-Lines from the Intracluster Medium of the Coma Cluster

Takuya SATO,[1] Kyoko MATSUSHITA,[1] Naomi OTA,[2] Kosuke SATO,[1] Kazuhiro NAKAZAWA,[3] and Craig L. SARAZIN[4]
[1] *Department of Physics, Tokyo University of Science, 1-3 Kagurazaka, Shinjuku-ku, Tokyo 162-8601*
j1209703@ed.kagu.tus.ac.jp, matusita@rs.kagu.tus.ac.jp
[2] *Department of Physics, Nara Women's University, Kitauoyanishi-machi, Nara, Nara 630-8506*
[3] *Department of Physics, The University of Tokyo, 7-3-1 Hongo, Bunkyo-ku, Tokyo 113-0033*
[4] *Department of Astronomy, University of Virginia, P.O. Box 400325, Charlottesville, VA 22904-4325, USA*

(Received 2011 June 9; accepted 2011 August 29)

Abstract

The Coma cluster was observed with the X-ray Imaging Spectrometer (XIS) onboard Suzaku in six pointings, including the central X-ray peak region, 14′ west offset region, 30′ and 34′ north–west offset regions, and 44′ and 60′ south–west offset regions. Owing to its lower background level, Suzaku has better sensitivity to Fe Kα lines than other satellites. Using precise Fe line measurements, we studied the temperature structure, possible bulk motions, and iron abundance distributions in the intracluster medium (ICM). The observed spectra were well-represented by a single-temperature model; a two- or three- temperature model did not improve χ^2 substantially. The temperature, derived from Kα line ratios of H-like and He-like Fe, agrees with those derived from the single-temperature model. Because the line ratio is a steep function of temperature, the consistency supports the accuracy of temperature measurements conducted with Suzaku. Within the 34′ region, the redshift derived from the central energy of the He-like Fe line is consistent with that from optical observations, within a calibration error of 18 eV or 818 km s^{-1} in the line of sight. This value is smaller than the sound velocity of the ICM, which is 1500 km s^{-1}. The central energy of Fe lines at the 44′ offset region around the NGC 4839 subcluster is also consistent with those within the 34′ region. These results on the temperature and velocity structure suggest that the core of the cluster is in a relaxed state, and non-thermal electrons relevant to the radio halo are accelerated by intracluster turbulence rather than large-scale shocks. The Fe abundance is almost constant at 0.4 solar within the 34′ region, and decreases with radius. This value is slightly lower than those of other clusters, which means that the gas had been mixed well during a past merger associated with the growth of the cluster.

Key words: galaxies: clusters: individual (Abell 1656, the Coma cluster) — galaxies: intergalactic medium — X-rays: galaxies: clusters

1. Introduction

Clusters of galaxies are thought to grow into larger systems through complex interactions between smaller systems. Signatures of merging events include temperature and density inhomogeneities and bulk motions in the intracluster medium (ICM). Numerical simulations predict simplified bulk motions with a substantial fraction of virial velocity (~ 1000 km s^{-1}), lasting several Gyr after each merging event (e.g., Roettiger et al. 1996; Norman & Bryan 1999). Measurements of the ICM temperature and velocity structure, therefore, provide crucial information for understanding the evolution of clusters.

Velocity measurements of bulk motion and turbulence are essential for mass estimation and cosmological studies. If ICM has a significant bulk velocity compared to its thermal velocity, the associated non-thermal pressure would threaten the assumption of hydrostatic equilibrium in deriving the total gravitational mass in a cluster. For example, factors of 2–3 discrepancies between the X-ray and lensing mass estimates in some objects (e.g., Ota et al. 2004; Hattori et al. 1999) could be partly due to this effect. Tamura et al. (2011) discovered a significant bulk motion in Abell 2256, which is a well-known merging cluster. Schuecker et al. (2004) performed a Fourier analysis of XMM-Newton data of the Coma cluster, which revealed the presence of a scale-invariant pressure fluctuation ranging between 29 and 64 kpc, and $\sim 10\%$ of the total pressure in turbulent form. However, in relaxed clusters, significant bulk motions and turbulence have not been detected. On the basis of ASCA and Chandra data, Dupke and Bregman (2001, 2006) claimed a large velocity gradient of ~ 2400 km s^{-1} in the Centaurus cluster, which is a relaxed cluster with a cool core. However, Ota et al. (2007) found a negative result of $|\Delta v| < 1400$ km s^{-1} on the basis of Suzaku observations of the Centaurus cluster. Sato et al. (2008) also searched for possible bulk motions in the AWM 7 cluster with Suzaku, and observed no significant bulk motions. The upper limit on the gas velocity was $|\Delta v| < 2000$ km s^{-1}. Fujita et al. (2008) did not detect any variation of the redshift of the ICM in the Ophiuchus cluster, and the upper limit of the velocity difference was 3000 km s^{-1}. Sugawara, Takizawa, and Nakazawa (2009) studied the ICM flow in Abell 2319 with Suzaku, and detected no velocity differences within the observed region. Using spectra with a Reflection Grating Spectrometer (RGS) onboard XMM-Newton, Sanders, Fabian, and Smith (2011) provided upper limits on turbulence velocities in cluster core regions; at least 15 sources had less than 20% of the thermal

energy density in turbulence.

The Coma cluster ($z = 0.0231$), also known as Abell 1656, is one of the most studied clusters (Biviano 1998), and has been observed at all wavelengths from radio to hard X-ray bands. However, the physical state, particularly the dynamical state, of the Coma cluster has not been completely understood. Measurements of the velocity dispersion and the distribution of galaxies belonging to the Coma cluster constrain the dynamical history of the Coma cluster. Fitchett and Webster (1987) found that two central galaxies, NGC 4889 and NGC 4874, have a significant difference in velocity, which is evidence of a recent merger. Colless and Dunn (1996) argued that NGC 4874 was the original dominant galaxy of the main cluster, and that NGC 4889 belonged to a subgroup that recently merged with the main cluster. A substructure associated with another galaxy, NGC 4839, located 40′ south–west of the cluster core, was found by Mellier et al. (1988) and Merritt and Trimbley (1994). The existence of this subcluster was confirmed by Colless and Dunn (1996).

The thermal X-ray emission of the Coma cluster has been observed with several X-ray satellites. Briel, Henry, and Böhringer (1992) constructed an X-ray map of the Coma cluster using ROSAT All-Sky-Survey data, and determined the X-ray surface brightness profile of the cluster out to a radius of roughly 100′. The temperature maps of clusters provide knowledge about the history of past subcluster mergers. On the basis of ASCA observations, Honda et al. (1996) and Watanabe et al. (1999) found that ICM is not isothermal. Arnaud et al. (2001) used XMM-Newton to study the temperature structure in the central region of the Coma cluster. The projected temperature distribution around NGC 4889 and NGC 4874 is remarkably homogeneous, which suggests that the core is mostly in a relaxed state. Except at the center, the temperature decreases slightly with radius. A cool filament of an X-ray emission in the direction of the galaxy NGC 4911, which is located south–east of the cluster center, was detected with Chandra (Vikhlinin et al. 1997) and XMM (Arnaud et al. 2001). ROSAT observed a substructure around the NGC 4839 subgroup (White et al. 1993), and a hot region in the direction of NGC 4839 was observed by Arnaud et al. (2001). By XMM-Newton observations, Neumann et al. (2001) found compelling evidence that the subgroup around NGC 4839 was on its first infall into the Coma cluster, but it had not yet passed its core. This interpretation is different from that of Burns et al. (1994), who suggested that the NGC 4839 group was moving out of the cluster after having already passed through the Coma cluster.

Non-thermal electrons, observed via diffused radio synchrotron emission, have been detected in more than 50 clusters, and all of them are undergoing mergers (e.g., Buote 2001; Schuecker et al. 2001). The Coma cluster also has a cluster-wide synchrotron radio halo, emitted by relativistic electrons due to merging (Feretti & Giovannini 1998). Recent non-thermal detections have been claimed by Rephaeli and Gruber (2002) with RXTE and by Fusco-Femiano et al. (2004, 1999) with BeppoSAX, although the latter detection is controversial (Rosetti & Molendi 2004; Fusco-Femiano et al. 2007). Long observations (~ 1 Ms) by INTEGRAL have imaged extended diffuse hard X-ray emission from the Coma cluster, although it was found to be completely consistent with thermal emission (Renaud et al. 2006; Eckert et al. 2007; Lutovinov et al. 2008). Using the temperature map of ICM obtained with the PN detector onboard XMM-Newton, Wik et al. (2009) analyzed data obtained from the Suzaku Hard X-ray Detector (HXD) (Takahashi et al. 2007) and derived the strongest upper limit of non-thermal emission.

This paper reports results from six Suzaku observations of the Coma cluster out to 60′, $\simeq 1.7$ Mpc, conducted using the X-ray Imaging Spectrometer (XIS) (Koyama et al. 2007) onboard Suzaku (Mitsuda et al. 2007). Owing to its lower background level, Suzaku has better sensitivity to the iron Kα lines than previous satellites. In addition, the accurate calibration of XIS allows us to measure the velocity of ICM precisely.

We used the Hubble constant, $H_0 = 70\,\mathrm{km\,s^{-1}\,Mpc^{-1}}$. The distance to the Coma cluster is $D_\mathrm{L} = 101$ Mpc, and 1′ corresponds to 28.9 kpc. We used the abundance ratio by Lodders (2003), in which the solar Fe abundance relative to H is 2.95×10^{-5}. Errors are quoted at the 90% confidence level for a single parameter.

The remainder of this paper is organized as follows: we present the observations in section 2 and describe the data analysis in section 3. We describe the results of spectral fittings and the temperature structure in subsection 4.1, bulk motions in subsection 4.5, and the Fe abundance in subsection 4.6. In section 5, we discuss the results, and in section 6, we summarize the findings.

2. Observation and Data Reduction

Suzaku carried out six observations in the Coma cluster. The details of the observations are summarized in table 1. Two central observations were carried out in 2006 May, during the Suzaku Phase-I period. The first observation, "Coma Radio Halo", has a pointing that is 5′ offset from the X-ray peak of the Coma cluster, which has coordinates (*RA*, *Dec*) = (194.9367, 27.9472) in degrees. The second observation, "Coma cluster offset", was located 14′ west offset from the first observation. The other observations, in the 30′ and 34′ north–west offset regions and 44′ and 60′ south–west offset regions, were carried out in 2007, during the Suzaku Phase-II period. To eliminate background emissions, archival Suzaku data with a 5° offset from the Coma cluster, observed in 2007 June, was also used, and shown in table 1.

XIS was operated in its normal mode during observations. The XIS instrument consists of four sets of X-ray CCD (XIS 0, 1, 2, and 3). XIS 1 is a back-illuminated (BI) sensor, while XIS 0, 2, and 3 are front-illuminated (FI) sensors. XIS 2 was not used during the four offset observations beyond 30′ from the X-ray peak. Figure 1 shows a 0.5–4.0 keV image of XIS 0.

We performed data reduction using HEAsoft version 6.6.3. XIS event lists created by the revision 2.0 pipeline processing were filtered using the following additional criteria: the geomagnetic cut-off rigidity (COR2) > 6 GV, and elevation angle from the Earth limb $> 10°$. The data formats of 5×5 and 3×3 editing modes were added. The exposure times after data selection are given in table 1.

To study the temperature structure and to search for possible bulk motions of ICM in the Coma cluster on a scale of a few

Table 1. Suzaku observation log of the Coma cluster.

Field name	Target name	Sequence number	Observation date	*RA* (°)	*Dec* (°)	Exposure (ks)	Distance from the X-ray peak*
center	Coma Radio Halo	801097010	2006-05-31	194.9267	27.9061	150	4′.7
14′ offset	Coma cluster offset	801044010	2006-05-30	194.6939	27.9466	79	13′.9
30′ offset	Coma 11	802082010	2007-06-19	194.6305	28.3939	53	30′.1
34′ offset	Coma BKG2	802084010	2007-06-21	194.3428	28.1403	30	33′.7
44′ offset	Coma 45	802047010	2007-12-02	194.2558	27.5714	30	44′.4
60′ offset	Coma 60	802048010	2007-12-04	194.0251	27.4252	35	59′.5
5° offset	Coma BKG	802083010	2007-06-21	198.7472	31.6480	30	4°.9

* X-ray peak has coordinates (*RA*, *Dec*) = (194.9367, 27.9472) in degrees.

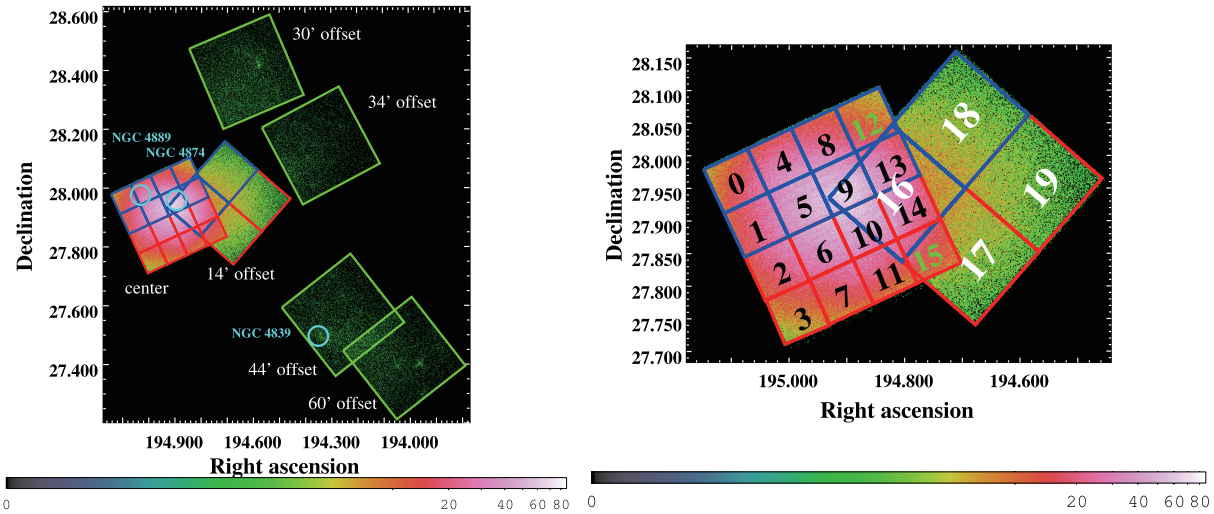

Fig. 1. XIS 0 image (0.5–4.0 keV) of the Coma cluster. Left: Differences in exposure time and the vignetting effect are uncorrected. Regions of spectral accumulation are shown as blue, red, and green squares. The light blue circles show the locations of NGC 4889, NGC 4874, and NGC 4839. Right: Definition of the cell numbers in the center and 14′ offset regions. The cell numbers 12 and 15 of the center region (green numbers) were excluded from our analysis because of strong emissions from calibration sources.

arcminutes, we divided the 18′ × 18′ square XIS field of view (FOV) of the center and 14′ offset regions into 4 × 4 and 2 × 2 cells, respectively, as shown in figure 1. Each region in the center and 14′ offset regions subtends 4′.5 × 4′.5 (130 kpc × 130 kpc), and 9′ × 9′ (260 kpc × 260 kpc), respectively. Regions around calibration sources were excluded. Luminous point sources in which the flux limit corresponds to $\sim 10^{-3}$ counts s^{-1} in the 2.0–10.0 keV energy range were also excluded as circular regions with a radius of 1′. At most, 10 point sources were excluded for each of the observed regions. We extracted spectra from the whole XIS FOV for regions more than $\geq 30'$ from the X-ray peak. The non-X-ray background (NXB) was subtracted from each spectrum using a database of night Earth observations with the same detector area and COR distribution (Tawa et al. 2008).

We included the degradation of energy resolution due to radiation damage in the redistribution matrix file (RMF) generated by the `xisrmfgen` Ftools task. We also created an ancillary response file (ARF) using the `xissimarfgen` Ftools task (Ishisaki et al. 2007). A decrease in the low-energy transmission of the XIS optical blocking filter (OBF) was also included in ARF. To generate ARF files for the center and 14′ offset regions, we used a β-model profile for the simulated surface brightness profile in Briel, Henry, and Böhringer (1992). For the 30′, 34′, 44′, 60′, and 5° offset regions, we generated ARFs assuming uniformly extended emission from an encircled region with a 20′ radius, because the gradient of surface brightness within each FOV is small. We used the XSPEC_v11.3.2ag package for spectral analysis.

3. Data Analysis

We have investigated the temperature structure, bulk motions, and iron abundance distribution of the Coma cluster. We fitted the spectra with a thermal plasma model (APEC: Smith et al. 2001) to obtain the temperature, redshift, and Fe abundance of ICM. A detailed spectral analysis is presented in subsection 3.2. We used three Gaussian models to obtain the temperature using the normalization ratio of Kα lines of H-like and He-like Fe, and redshift using the shift of line centroid energy, which is presented in subsection 3.3.

Table 2. Resultant parameters of fits in the background region.

Cosmic X-ray background		Local hot bubble		Milky Way halo			
Γ	Normalization*	Temperature (keV)	Normalization† ($\times 10^{-3}$)	Temperature (keV)	Normalization† ($\times 10^{-4}$)	Reduced-χ^2 χ^2/d.o.f.‡	χ^2/d.o.f.§
1.38 ± 0.07	7.6 ± 0.3	0.07 (fixed)	6.79 ± 2.57	0.16 ± 0.03	6.55 ± 2.57	188/141	223/154

* Units: photons $\mathrm{cm^{-2}\,s^{-1}\,keV^{-1}\,sr^{-1}}$ at 1 keV.
† Normalization of the APEC component divided by the solid angle, Ω^{U}, assumed in the uniform-sky ARF calculation (20′ radius), normalization $= \int n_{\mathrm{e}} n_{\mathrm{H}} dV/[4\pi(1+z)^2 D_{\mathrm{A}}^2]/\Omega^{\mathrm{U}} \times 10^{-14}\,\mathrm{cm^{-5}}\,(400\pi)^{-1}\,\mathrm{arcmin^{-2}}$, where D_{A} is the angular distance to the source.
‡ Resultant χ^2/d.o.f. fitted excluding 1.40–1.55 keV.
§ Resultant χ^2/d.o.f. fitted including 1.40–1.55 keV.

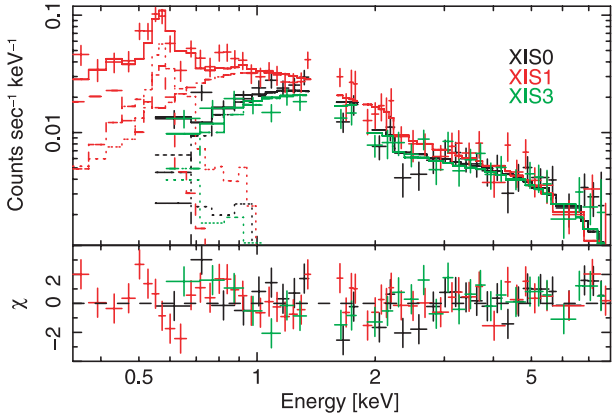

Fig. 2. NXB-subtracted spectra of the 5° offset region in the 0.3–8.0 (red: XIS 1) and 0.5–8.0 keV energy ranges (black and green for XIS 0 and 3, respectively), ignoring the 1.40–1.55 keV energy range, where a relatively large uncertainty exists in the instrument background (Tawa et al. 2008). The bottom panel shows the residuals of the fit.

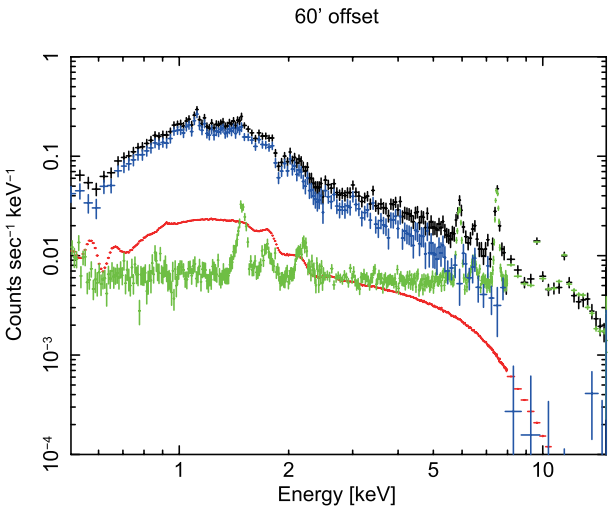

Fig. 3. XIS 0 spectra of the 60′ offset region of the Coma cluster (black), NXB (green), and the simulated background spectrum including LHB, MWH, and CXB (red). Blue crosses show the background-subtracted spectrum of the 60′ offset region of the Coma cluster.

3.1. *Estimation of Background Spectra*

First, we fitted the spectra in the 5° offset region to determine the local X-ray background. As shown in Yoshino et al. (2009), the background emission of Suzaku XIS can be fitted with a three-component model: two thermal plasma models (APEC: Smith et al. 2001) for the local hot bubble (LHB) and the Milky Way halo (MWH), and a power-law model for the extragalactic cosmic X-ray background (CXB). MWH and CXB components were convolved with absorption in the Galaxy. We, therefore, fitted the spectra simultaneously in the 0.5–8.0 keV energy range for XIS FIs and the 0.35–8.0 keV energy range for XIS BI using the following model formula: $\mathrm{apec_{LHB}} + \mathrm{wabs} \times (\mathrm{apec_{MWH}} + \mathrm{power\text{-}law_{CXB}})$. We assumed a zero redshift and a solar abundance for LHB and MWH components. The temperature of LHB was fixed at 0.07 keV (Takei et al. 2008), while the temperature of MWH was variable. The column density of the Galactic neutral hydrogen was fixed at $1.0 \times 10^{20}\,\mathrm{cm^{-2}}$ (Kalberla et al. 2005). To avoid systematic uncertainties in the background, we ignored the 1.40–1.55 keV energy range, where a relatively large uncertainty exists because of an instrument Al line (Tawa et al. 2008), and energies above 8 keV. We also excluded the narrow energy band between 1.82 and 1.84 keV in the fits because of incomplete responses around the Si edge. Results of the spectral fit are shown in figure 2 and the resultant parameters of the fit are given in table 2. The derived photon index and normalization of the CXB component agree with Kushino et al. (2002) and Takei et al. (2008). The derived temperature and normalizations of the two thermal models are consistent with those obtained from XMM and Suzaku observations (Lumb et al. 2002; Yoshino et al. 2009).

We generated the simulated spectra of the X-ray background including LHB, MWH, and CXB emissions derived from the resultant parameters of the fits in the 5° offset region. We used the simulated spectra as the background to fit the spectra for ICM of the Coma cluster. Figure 3 shows a comparison between the XIS 0 spectra of the 60′ offset region of the Coma cluster and backgrounds. Above 7 keV, NXB dominates the observed spectra of the 60′ offset region. We also show the background-subtracted spectrum of the 60′ offset region of the Coma cluster in figure 3 (blue). The X-ray background spectra are well reproduced.

3.2. *Spectral Fits with Single-, Two-, and Three-Temperature Models*

We fitted the XIS spectra in each region of the Coma cluster using a single-temperature model (APEC) with the

Table 3. Resultant parameters of the fits with the single-temperature (APEC) model in the energy ranges of 1.0–8.0 keV and 5.0–8.0 keV, the two- or three-temperature model, and three Gaussians models.*

	APEC fit in 1.0–8.0 keV					APEC fit in 5.0–8.0 keV			Gaussians
Region	kT (keV)	χ^2/d.o.f.† ($1T$)	χ^2/d.o.f.‡ ($1T$)	χ^2/d.o.f.§ ($2T$)	χ^2/d.o.f.‖ ($3T$)	Fe (solar)	Redshift ($\times 10^{-2}$)	χ^2/d.o.f.	kT from line ratio (keV)
Center									
0	$8.47^{+0.14}_{-0.08}$	938/ 829	776/711	772/709	770/707	$0.47^{+0.06}_{-0.05}$	$2.17^{+0.16}_{-0.16}$	265/244	$8.08^{+0.80}_{-0.80}$
1	$7.81^{+0.09}_{-0.10}$	1373/1108	1037/950	999/948	996/946	$0.40^{+0.02}_{-0.04}$	$2.24^{+0.09}_{-0.10}$	319/328	$7.75^{+0.51}_{-0.48}$
2	$7.19^{+0.11}_{-0.09}$	1325/1108	1015/950	1007/948	1004/946	$0.39^{+0.03}_{-0.03}$	$2.09^{+0.11}_{-0.10}$	344/328	$6.86^{+0.52}_{-0.52}$
3	$7.12^{+0.18}_{-0.19}$	901/ 829	728/711	728/709	726/707	$0.33^{+0.04}_{-0.09}$	$2.11^{+0.19}_{-0.09}$	245/244	$6.78^{+0.94}_{-0.91}$
4	$8.73^{+0.12}_{-0.16}$	1363/1108	1082/950	1075/948	1075/946	$0.37^{+0.03}_{-0.03}$	$2.42^{+0.09}_{-0.12}$	352/328	$8.61^{+0.56}_{-0.54}$
5	$8.20^{+0.07}_{-0.07}$	1574/1108	1105/950	1082/948	1081/946	$0.40^{+0.03}_{-0.02}$	$2.25^{+0.07}_{-0.08}$	394/328	$8.25^{+0.38}_{-0.37}$
6	$7.81^{+0.08}_{-0.07}$	1298/1108	994/950	962/948	961/946	$0.42^{+0.02}_{-0.03}$	$2.14^{+0.08}_{-0.07}$	346/328	$8.17^{+0.40}_{-0.40}$
7	$7.45^{+0.11}_{-0.12}$	1314/1108	1018/950	975/948	971/946	$0.48^{+0.04}_{-0.05}$	$2.23^{+0.19}_{-0.13}$	333/328	$7.70^{+0.63}_{-0.67}$
8	$8.93^{+0.15}_{-0.15}$	1290/1108	994/950	993/948	993/946	$0.38^{+0.04}_{-0.04}$	$2.42^{+0.14}_{-0.10}$	390/328	$9.45^{+0.66}_{-0.63}$
9	$8.66^{+0.09}_{-0.12}$	1533/1108	1049/950	1000/948	999/946	$0.40^{+0.01}_{-0.02}$	$2.33^{+0.08}_{-0.02}$	318/328	$8.93^{+0.41}_{-0.40}$
10	$8.26^{+0.07}_{-0.07}$	1395/1108	1005/950	975/948	968/946	$0.38^{+0.02}_{-0.03}$	$2.14^{+0.07}_{-0.08}$	349/328	$8.31^{+0.41}_{-0.41}$
11	$8.15^{+0.13}_{-0.13}$	1379/1108	1068/950	1041/948	1041/946	$0.37^{+0.04}_{-0.04}$	$2.21^{+0.15}_{-0.12}$	369/328	$8.23^{+0.65}_{-0.65}$
13	$9.08^{+0.15}_{-0.23}$	1361/1108	1106/950	1103/948	1103/946	$0.33^{+0.04}_{-0.03}$	$2.33^{+0.13}_{-0.12}$	378/328	$9.23^{+0.66}_{-0.74}$
14	$8.95^{+0.15}_{-0.16}$	1306/1108	1046/950	1029/948	1029/946	$0.39^{+0.04}_{-0.04}$	$2.31^{+0.15}_{-0.14}$	357/328	$8.96^{+0.71}_{-0.71}$
14′ offset									
16	$9.14^{+0.13}_{-0.14}$	1355/1108	1047/950	1035/948	1035/946	$0.40^{+0.03}_{-0.03}$	$2.38^{+0.08}_{-0.07}$	352/328	$8.83^{+0.54}_{-0.54}$
17	$9.22^{+0.19}_{-0.10}$	1201/1108	987/950	974/948	967/946	$0.34^{+0.04}_{-0.05}$	$2.21^{+0.18}_{-0.08}$	332/328	$9.29^{+0.92}_{-0.89}$
18	$9.00^{+0.19}_{-0.22}$	1303/1108	1087/950	1078/948	1077/946	$0.36^{+0.05}_{-0.07}$	$2.39^{+0.13}_{-0.24}$	396/328	$9.22^{+0.89}_{-0.89}$
19	$8.43^{+0.16}_{-0.17}$	1280/1108	1067/950	1054/948	1054/946	$0.27^{+0.05}_{-0.05}$	$2.23^{+0.22}_{-0.25}$	389/328	$7.82^{+1.18}_{-1.17}$
30′ offset	$6.65^{+0.29}_{-0.25}$	452/ 397	387/343	370/341	368/339	$0.26^{+0.06}_{-0.13}$	$2.30^{+0.45}_{-0.43}$	135/ 94	$7.29^{+2.74}_{-2.76}$
34′ offset	$8.46^{+0.67}_{-0.46}$	484/ 397	408/343	405/341	405/339	$0.21^{+0.13}_{-0.10}$	$1.92^{+1.10}_{-1.07}$	107/ 94	$7.67^{+1.74}_{-1.72}$
44′ offset	$5.31^{+0.20}_{-0.15}$	445/ 397	360/343	350/341	349/339	$0.37^{+0.09}_{-0.08}$	$2.69^{+0.33}_{-0.30}$	106/ 94	$6.33^{+1.64}_{-1.63}$
60′ offset	$3.74^{+0.13}_{-0.13}$	401/ 397	344/343	344/341	325/339	$0.29^{+0.10}_{-0.10}$	$2.67^{+0.50}_{-0.51}$	93/ 94	2.19 (<5.95)

* In the case of three Gaussian models, we converted the normalization ratio of Kα lines of H-like and He-like Fe to temperature with the APEC model.
† χ^2/d.o.f. of single-temperature spectral fits including the 1.7–2.3 keV energy range.
‡ χ^2/d.o.f. of single-temperature spectral fits excluding the 1.7–2.3 keV energy range.
§ χ^2/d.o.f. of two-temperature spectral fits excluding the 1.7–2.3 keV energy range.
‖ χ^2/d.o.f. of three-temperature spectral fits excluding the 1.7–2.3 keV energy range.

Galactic absorption, $N_{\rm H}$. Each spectral bin contained 50 or more counts. We fitted the spectra in two energy bands: 1.0–8.0 and 5.0–8.0 keV. To avoid systematic uncertainties in the background, we ignored energies higher than 8 keV. We also excluded the narrow energy band between 1.82 and 1.84 keV in the fits because of incomplete responses around the Si edge. The temperature, redshift, and normalization of the single-temperature model were free parameters, and $N_{\rm H}$ was fixed to the Galactic value, 1.0×10^{20} cm^{-2}, in the direction of the Coma cluster. The abundances of He, C, N, and Al were fixed to be solar. We divided the other metals into three groups: O, Ne, and Mg; Si, S, Ar, and Ca; and Fe and Ni, and allowed them to vary. The resultant parameters are summarized in table 3, and a sample of the spectra is shown in figure 4. Since our data have very high statistics, especially in the central region, there remain residual structures around the Si edge structure. These residuals are probably caused by systematic uncertainties in the response matrix because the BI and FI detectors gave different residuals. Therefore, to avoid systematic uncertainties in all regions, we excluded the energy range of 1.7–2.3 keV and fitted the spectra again. The derived temperatures hardly changed, although the reduced χ^2 decreased by 20%. The resultant χ^2 values are summarized in table 3.

To constrain the temperature structure, we fitted the spectra of the center and offset regions with a two-temperature (APEC) model in the energy range of 1.0–8.0 keV, ignoring the energy range of 1.7–2.3 keV. The χ^2 are improved slightly by less

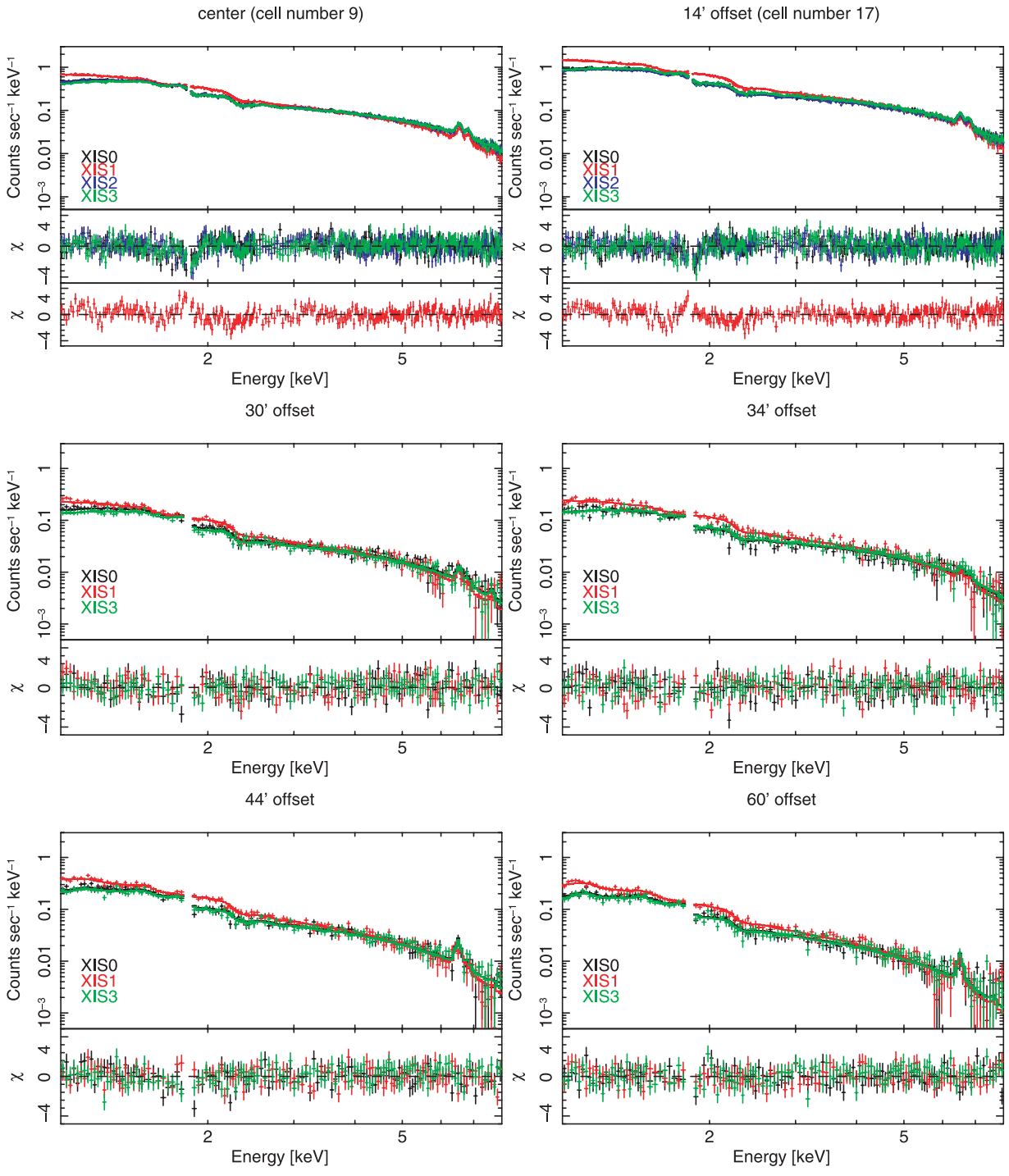

Fig. 4. Spectra for one cell in the center and 14′ offset regions, and all other offset regions, fitted by the single-temperature (APEC) model. Black, red, blue, and green crosses and lines correspond to the XIS 0, 1, 2, and 3, respectively. The middle and bottom panels show the residuals of the fit.

than a few percent. The derived temperatures of one component are similar to those derived from the single-temperature model fits, and those of the other component are either above 10 keV or below 2 keV. To obtain more detailed constraints for the lower and higher temperature components, we fitted the spectra with a three-temperature (APEC) model in the energy range of 1.0–8.0 keV, excluding the 1.7–2.3 keV energy range to avoid uncertainties in the response matrix. In this model, the lowest, middle, and highest temperatures are restricted to below 6 keV, within 6.0–10.0 keV, and above 10.0 keV, respectively. The resultant χ^2 values are shown in table 3.

To derive the Fe abundance and the velocity of the bulk-motion from the Fe-K lines, we fitted the spectra of each region with the single-temperature APEC model in an energy range of

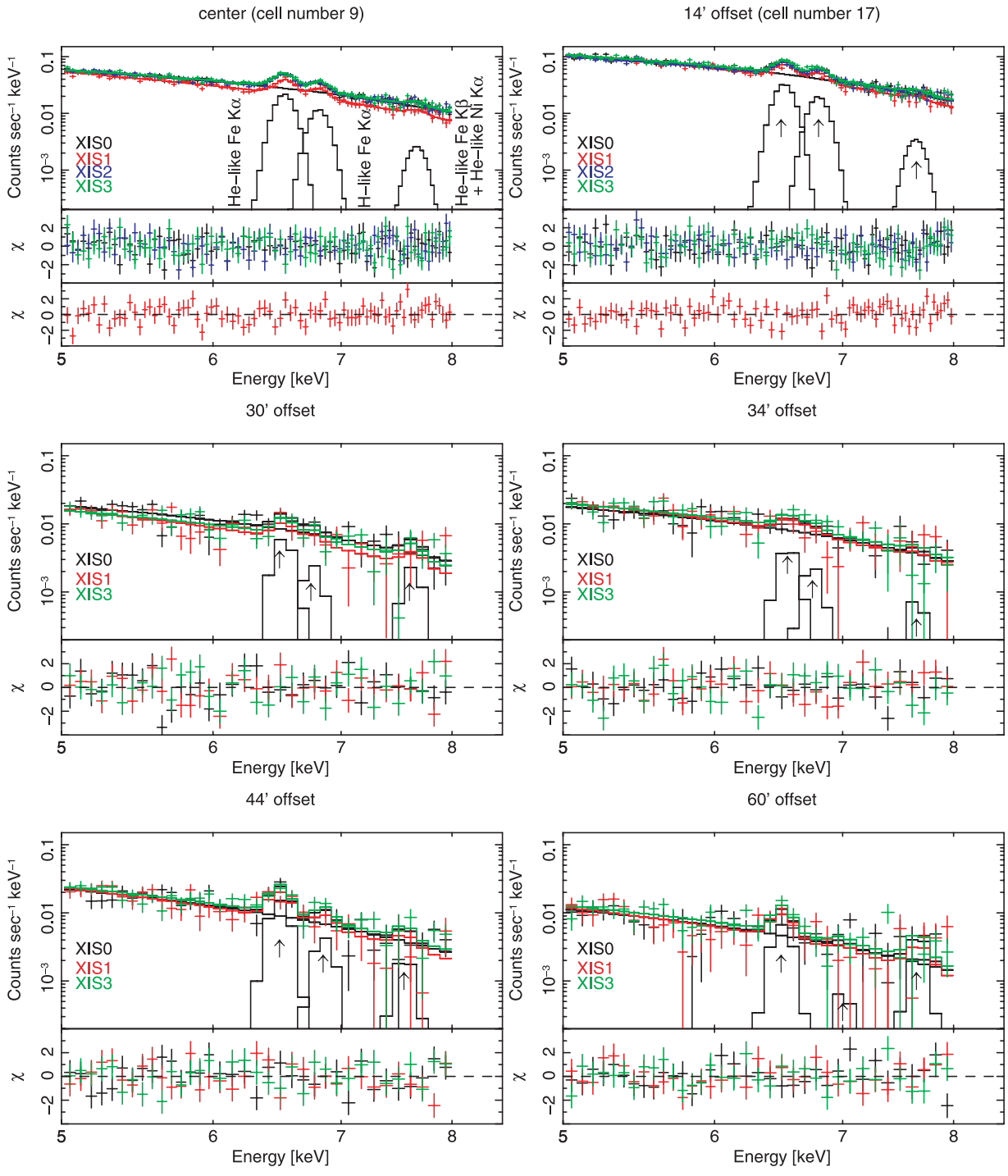

Fig. 5. Representative iron Kα line spectra (for the same regions as in figure 4), fitted with the bremsstrahlung and three Gaussian models in the energy range of 5.0–8.0 keV. Three Gaussian models (black lines) represent the strong Kα line of He-like Fe, a weaker line of H-like Fe, and a mixture of the Kα line of He-like Ni and the Kβ line of He-like Fe.

5.0–8.0 keV. The results are given in table 3.

To precisely determine the bulk velocity of ICM, the accuracy of photon energy measurements is crucial. Some sensors have large uncertainties in the determination of the line centroid energy. Thus, we averaged the spectrum over FOV in (i) all detectors, and (ii) all detectors, except for different Mn Kα line centroid energies, to check the spectral shape and measured redshift in the center and NGC 4839 regions (44′ offset region).

3.3. *Central Energy and Normalization Ratio of Fe Lines*

To derive the ICM temperature from the normalization ratio of Kα lines of H-like and He-like Fe, and the possible bulk motions of ICM from the central energy of the lines, we fitted

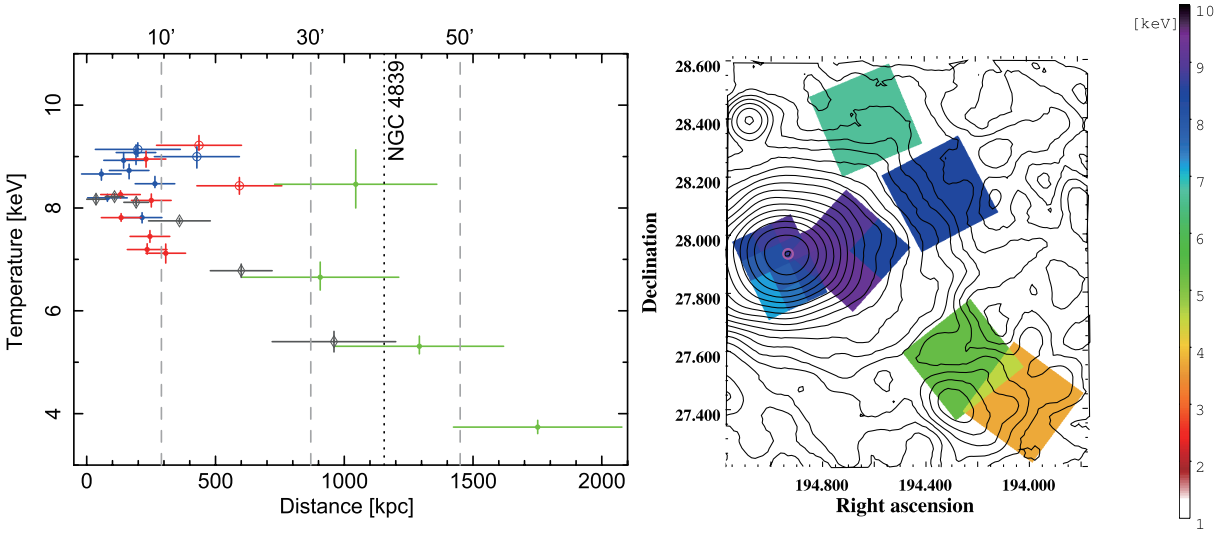

Fig. 6. Radial temperature profile from the X-ray peak (left) and temperature map (right) from our observations of the Coma cluster. Temperatures are derived from the spectral fits with the single-temperature (APEC) model in the energy range of 1.0–8.0 keV. The color notations in the left panel are the same as those in figure 1. Open and filled circles correspond to the center and 14′ offset regions, respectively, and gray diamonds indicate the results from XMM-Newton (Matsushita 2011). The magenta circle in the right panel shows the X-ray peak of the Coma cluster. The temperature map is overlaid on X-ray contours on a linear scale in the 0.4–2.4 keV energy range from the ROSAT-All-Sky-Survey.

the spectra in the energy range of 5.0–8.0 keV with a sum of bremsstrahlung and three Gaussian components, which correspond to Kα lines of He-like and H-like Fe, and a mixture of the Kα line of He-like Ni and the Kβ line of He-like Fe. The temperature and normalization of the bremsstrahlung component, and the central energy and normalizations of the Gaussian components were free parameters, while the line width of Gaussian models was fixed at 0. The best-fit spectra are shown in figure 5.

4. Results

4.1. Temperature Structure of ICM

Figure 6 shows a radial profile and map of the derived temperatures from the spectral fits with the single-temperature (APEC) model in the energy range of 1.0–8.0 keV. The radial temperature profile of the Coma cluster is relatively flat within $\sim$500 kpc, which corresponds to the 14′ offset region, and decreases with the radius to the outer region. While the regions observed with Suzaku are limited, the resultant temperature profile is similar to that derived from XMM-Newton observations, which cover nearly the entire Coma cluster out to $\sim$1200 kpc (Matsushita 2011).

Excluding the south–east quadrant (cell numbers: 2, 3, 6, and 7), and the 14′ offset region, the temperatures of cells in the center region have a flat distribution within a small range between $\sim$8 keV and $\sim$9 keV. Within 300 kpc from the X-ray peak in the center region, the weighted mean temperature with statistical errors of the 14 cells is 8.34 ± 0.19 keV. The south–east quadrant (cell numbers: 2, 3, 6, and 7) in the center region has a slightly cooler temperature: the weighted average with statistical errors of the four cells is 7.39 ± 0.11 keV. This value is close to that of 5.0–7.0 keV in the cool temperature region observed by XMM-Newton, which would be a counterpart of the south–east quadrant region (Arnaud et al. 2001). On the other hand, the north–west part in the center region (cell numbers: 8, 13, and 14) and the nearby area of the 14′ offset region (cell numbers: 16, 17, 18) have slightly higher temperatures of $\sim$9 keV. The 34′ offset region, located to the north–west of the 14′ offset region, also has a relatively high temperature of $\sim$8–9 keV. This direction corresponds to the hot spot, $kT = 12.7^{+3.6}_{-2.0}$ keV in Donnelly et al. (1999) with ASCA, and $kT = 8.4 \pm 0.4$ keV in Arnaud et al. (2001) with XMM-Newton. Recent INTEGRAL observations have shown a surface brightness excess relative to XMM observations, which is well-represented by extended hot thermal emission with $\sim 12 \pm 2$ keV (Eckert et al. 2007). The temperature in the 30′ offset region is around $\sim$6–7 keV, and is clearly cooler than temperatures in the inner region. This value is consistent with the previous results in Honda et al. (1996), and Takei et al. (2008).

The 44′ and 60′ offset regions include the NGC 4839 subcluster, and the temperatures decrease with radius to 5.31 ± 0.20 keV and 3.74 ± 0.13 keV, respectively. These values are cooler than those in Honda et al. (1996) with ASCA, but are consistent with those in Wik et al. (2009) and Neumann et al. (2001) with XMM-Newton. The temperatures of the core and tail of NGC 4839 with XMM-Newton, which is located in the 44′ offset region with Suzaku, are $3.1^{+3.7}_{-2.4}$ keV and $4.8^{+6.0}_{-4.0}$ keV, respectively (Neumann et al. 2001). The temperature of the main body of the subcluster is $4.4^{+4.0}_{-4.7}$ keV (Neumann et al. 2001). Suzaku provided more significant temperatures than previous measurements in these regions.

In summary, the temperature distribution observed with Suzaku is fairly consistent with the previous results observed with ASCA, XMM, and INTEGRAL. In addition, we note that the statistical and systematic errors with Suzaku are much smaller than those in previous results.

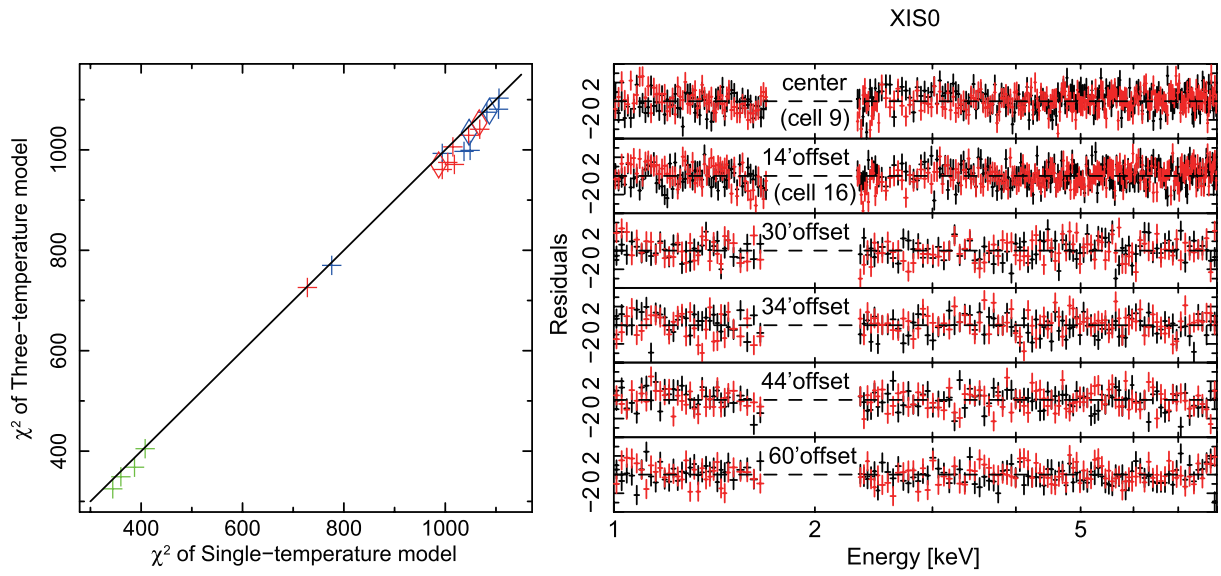

Fig. 7. Left: Comparison of χ^2 fitted with the single- and three-temperature (APEC) models. Color notations are the same as those in figure 1. Right: Residuals of the fit of XIS 0 with single-temperature (black) and three-temperature (red) models versus energy. Each panel shows the region of the spectral fit.

4.2. Fits with Three-Temperature Models

As shown in figure 4, the spectra in the energy range of 1.0–8.0 keV are well-represented by the single-temperature model. Except for discrepancies between FI and BI detectors around the Si-edge, there are no systematic residuals. Figure 7 shows a comparison of the resultant χ^2 fitted with the single- and three-temperature (APEC) models in the energy range of 1.0–8.0 keV, excluding the 1.7–2.3 keV energy range. A more statistically rigorous approach would be to apply the f-test to compare the single-temperature and three temperature models. The f-test indicates that the three-temperature model is significantly better than the single-temperature model in regions 1, 5, 6, 7, 9, 10, and 11 of the center region and 17 of the 14′ offset region, and better in regions 2 and 14 of the center region, and 16 and 19 of the 14′ offset region, the 30′ offset region, 44′ offset region, and 60′ offset region. The largest f statistic value is 11.4 in cell number 7 of the center region, and the least f statistic value is 0.238 in cell number 8 of the center region. However, the single-temperature model fit still represents the spectra fairly well.

4.3. Temperatures Derived from Fe Line Ratios

The spectra accumulated over each region may contain multi temperature components, although the single-temperature (APEC) model represented those spectra well. Because the ratio of He-like and H-like Fe Kα lines strongly depends on the plasma temperature, comparisons of temperatures derived from the line ratio and spectral fits with the thermal model are useful for understanding the temperature structure of ICM. Figure 8 shows the ratios of the resultant normalizations of the Fe Kα lines, plotted versus the temperature derived from the spectral fits with the single-temperature (APEC) model in the energy range of 1.0–8.0 keV. To convert line ratios to plasma temperature, we generated mock spectra assuming the single-temperature APEC or MEKAL (Mewe et al. 1985, 1986; J. S. Kaastra 1992;[1] Liedahl et al. 1995) plasma code models, convolved with XIS energy resolution. We then fitted the mock spectra with a sum of a bremsstrahlung and three Gaussian models. The theoretical line ratios from APEC and MEKAL plasma codes are also plotted in figure 8. The derived line ratios agreed with these theoretical line ratios of the APEC plasma code assuming the single-temperature model, while the MEKAL model gave a line ratio value several percent lower at a given temperature. Assuming a single-temperature plasma, we converted the observed line ratios to plasma temperatures using the theoretical relation for the APEC model. Results are given in table 3 and figure 8. As shown in figure 8, line temperatures agreed with those derived from the spectral fits very well.

4.4. Temperatures at the Edge of the Radio Halo

Brown and Rudnick (2011) claimed a significant temperature difference of ICM at the edge of the radio halo on the basis of XMM-Newton observations: the temperature at the inner edge of the radio halo is 6.8 ± 0.6 keV, while the temperature at the outer edge of the radio halo is 16.3 ± 2.9 keV. To examine this temperature difference, we extracted spectra from counterpart regions in the 34′ offset region, which are represented by two red boxes in figure 9, and fitted the spectra with the single-temperature (APEC) model. As shown in figure 9, there are no significant temperature differences for each box in the 34′ offset region. We then divided FOV of the 34′ offset region into 2×2 cells as shown in figure 9, and fitted the spectra with the single-temperature (APEC) model. The derived temperatures are also consistent with each other.

[1] An X-Ray Spectral Code for Optically thin Plasmas, Internal SRON-Leiden Report, Ver. 2.

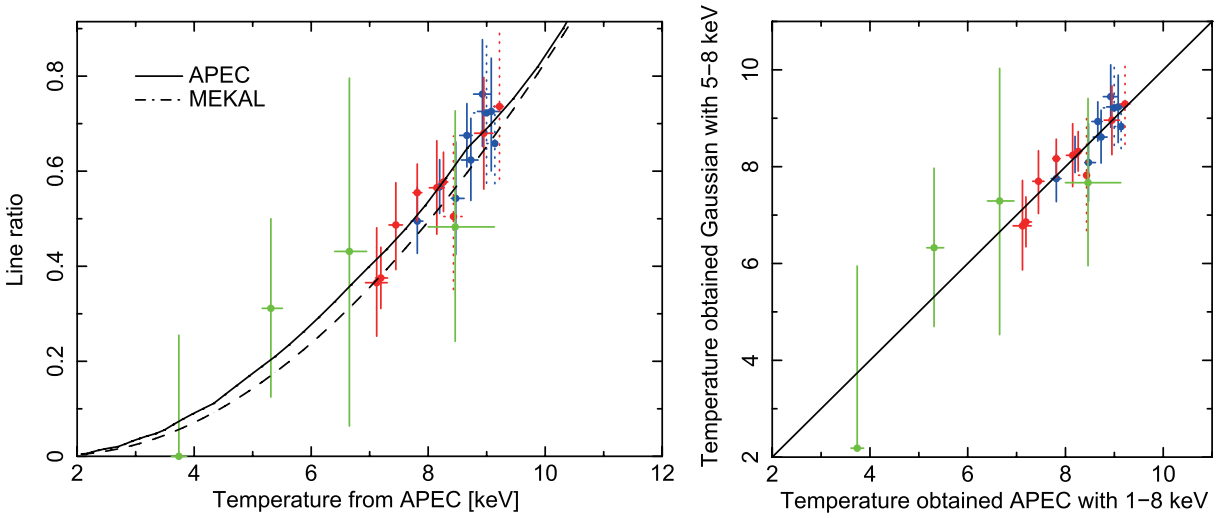

Fig. 8. Left: Comparison between ratios of the normalizations of the Fe Kα lines of H-like and He-like Fe and the temperatures derived from the spectral fits with the single-temperature (APEC) model in the energy range of 1.0–8.0 keV. Filled blue and red circles with solid error bars correspond to the results of the north and south cells in the center region, respectively. Those with dashed error bars show the results of northeast and southwest cells in the 14′ offset region, respectively. Green circles indicate the results of the four offset regions. The solid and dashed black curves show the theoretical relation between the line ratio and plasma temperature from APEC and MEKAL codes, respectively. Right: Comparison of temperatures derived from line ratios of the Fe Kα lines and spectral fits with the single-temperature (APEC) model in the energy range of 1.0–8.0 keV.

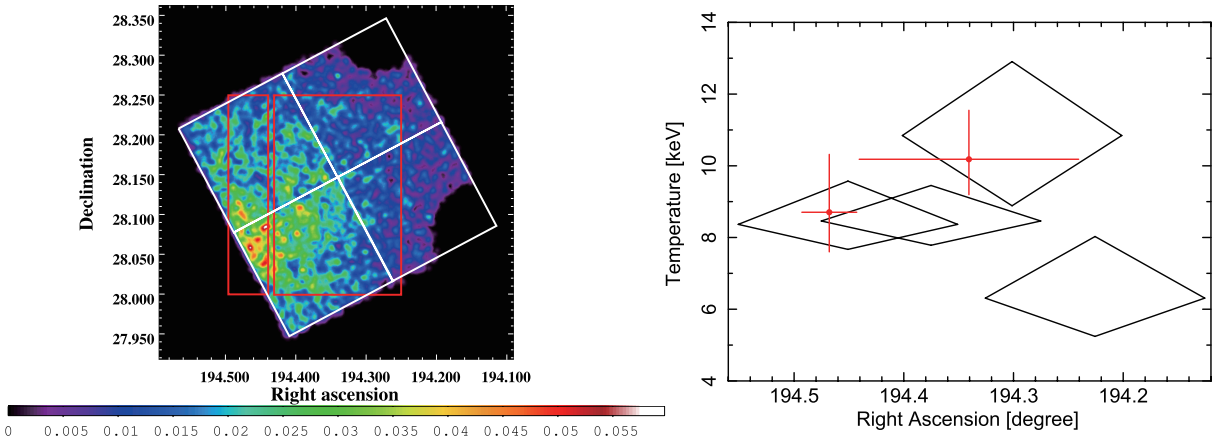

Fig. 9. Left: XIS 0 image of the 34′ offset region. Red and white squares indicate spectral extraction regions. Right: Temperatures of ICM in the 34′ offset region, plotted versus right ascension. Red crosses and black diamonds correspond to the red and white squares, respectively.

4.5. Search for ICM Bulk Motions

4.5.1. Systematic uncertainty in the energy scale

To constrain the line-of-sight gas motion using the He-like Fe-Kα line, precise calibration of the XIS energy scale is crucial. Because the six data sets used in the present analysis have three different observation epochs (2006 May, 2009 June, and 2009 December), it is necessary to check the energy scale for each observation. In addition, the energy gain may vary from place to place on the same CCD chip owing to the charge transfer inefficiency. We thus estimated the XIS calibration uncertainty in the following two ways: (i) measurements of the calibration source energy and (ii) comparisons of redshift values derived from four or three sets of XIS CCD.

(i) The fiducial absolute energy scale can be examined by measuring the centroid energy of the Mn Kα line from built-in calibration sources, which illuminate two corners of each XIS CCD. The spectra accumulated from the calibration source regions were fitted to the power-law model for continuum and two Gaussian functions for the Mn Kα line at 5.894 keV and Mn Kβ line at 6.490 keV. Because the Mn Kβ line has an intrinsically complex line shape and is contaminated by the cluster iron emission, only the Mn Kα line was used for the calibration. Figures 10 and 11 show the result of spectral fitting and the Mn Kα line centroid energy, respectively.

As shown in the left panel of figure 11, the measured line energies for the center or 14′ offset regions are systematically lower than the Mn Kα line energy by 7.3 eV if they are averaged over four sensors and two detector segments in each pointing. For XIS 3, centroid energies are lower than

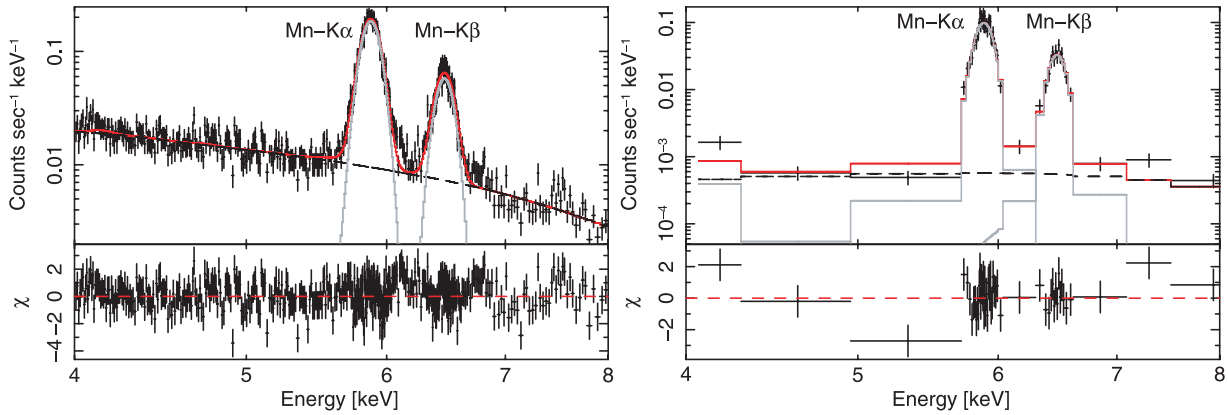

Fig. 10. Observed XIS 0 spectrum (black crosses) in the energy range around the calibration source for the center (left) and 30′ offset (right) regions fitted with the power-law and two Gaussian models. The solid (red) line shows the best-fit model and the dashed and solid gray lines indicate the power-law and Gaussian models, respectively. Mn-Kα, Mn-Kβ lines, and Fe lines from the cluster emission are seen in this spectrum. The lower panels show the residual of the fits.

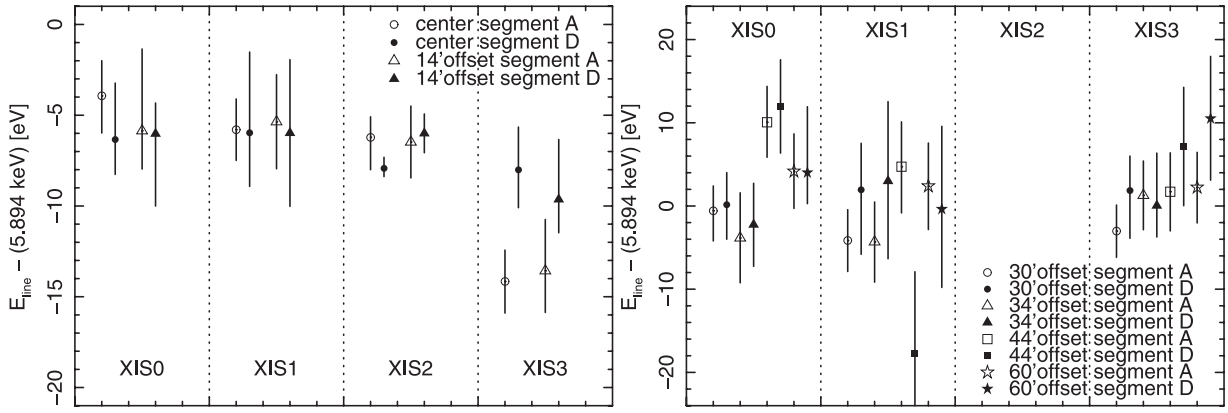

Fig. 11. Left: Resultant residuals of the central energy of the Mn-Kα line (5.894 keV) for the center and 14′ offset regions. Open and filled symbols show the segments A and D on XIS CCD, respectively. Right: Same as the left panel for the 30′, 34′, 44′, and 60′ offset regions.

those of the other three chips, however, we confirmed that the spectral analysis of the redshift measurement with and without XIS 3 gave statistically consistent results (see subsubsection 4.5.3 for more details). We then estimated the $1\,\sigma$ systematic uncertainty on the energy scale to be $\sigma_{\rm sys,Mn} = 7$ eV, which is derived from the measured Mn Kα line centroid E_i and the $1\,\sigma$ statistical error σ_i for the XIS-i detector, and the Mn Kα line energy in literature $\langle E \rangle$. χ^2 is defined as $\chi^2 = \sum_{\rm seg} \sum_{i=0}^{3} (E_i - \langle E \rangle)^2 / (\sigma_i^2 + \sigma_{\rm sys,Mn}^2)$. With $\sigma_{\rm sys,Mn} = 7$ eV, χ^2 becomes less than 10 for 7 degrees of freedom, which means the probability of χ^2 exceeding χ^2 versus the number of degrees of freedom becomes less than 10%: the number of bins is 8 for four sensors and two detector segments, and E can be regarded as being consistent with $\langle E \rangle$ when we consider $\sigma_{\rm sys,Mn} = 7$ eV. In the same manner, the systematic errors are obtained as $\sigma_{\rm sys,Mn} = 1$ eV, 1 eV, 6 eV, 4 eV for the 30′, 34′, 44′, and 60′ offset regions, respectively. Therefore, for safety's sake, we assign 7 eV for the $1\,\sigma$ (68% confidence level) gain uncertainty.

(ii) Though calibration sources provide information on the absolute energy scale at the corners of CCD chips, the gain may be dependent on the position. This intrachip variation can be effectively studied by comparing the line energies of the same sky regions (which correspond to different detector regions) on four or three XIS sensors (see also subsection 3.1 in Ota et al. 2007). To examine this issue, we divided the center region into 16 cells, and fitted the APEC model in the energy range of 5.0–8.0 keV for each XIS sensor. We then estimated the $1\,\sigma$ systematic error with a reference to obtain the redshift, calculating as $\chi^2 = \sum_{k=0}^{15} \sum_{i=0}^{3} (E_{z_k,(\text{XIS-}i)} - \langle E_{z_k} \rangle)^2 / ({\sigma_k^{(\text{XIS-}i)}}^2 + \sigma_{\rm sys}^2)$ for each pair of XIS sensors, where $E_{z_k,(\text{XIS-}i)}$ is the measured line centroid for the XIS-i detector in each region; $\langle E_{z_k} \rangle$ is the mean of the line centroid for all XIS-i detectors in each region, and $\sigma_k^{(\text{XIS-}i)}$ is the $1\,\sigma$ statistical error in the XIS-i detector. With $\sigma_{\rm sys} = 11$ eV, χ^2 becomes less than 17 for 11 degrees of freedom, which means the probability of χ^2 exceeding χ^2 versus the number of degrees of freedom becomes less than 10%: the number of bins is 12 for the spectral regions, except for the calibration source regions in the center region. $\sigma_k^{(\text{XIS-}i)}$ is ~ 10 eV, which is larger than the gain uncertainty: thus, we ignored $\sigma_k^{(\text{XIS-}i)}$ to avoid underestimating the systematic

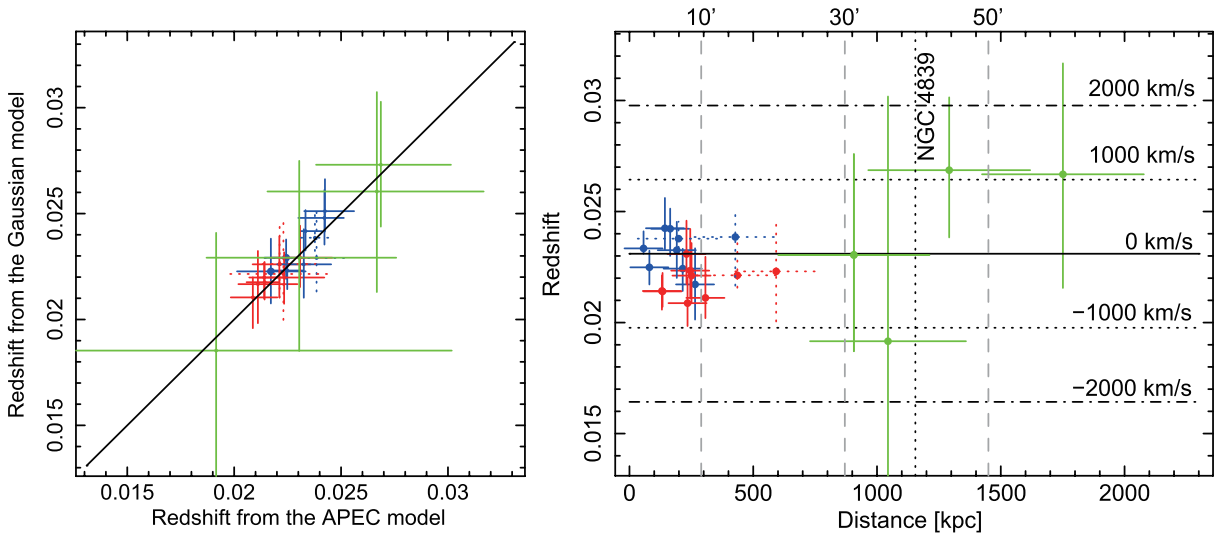

Fig. 12. Left: Comparison of redshifts derived from spectral fits with the single temperature (APEC) model in the 5.0–8.0 keV energy range, and the shifted centroid energy of the He-like Fe Kα line. Right: Derived redshifts with the single temperature (APEC) model in the 5.0–8.0 keV energy range, plotted versus the distance from the X-ray peak of the Coma cluster. Color notations are the same as in figure 1. The solid line corresponds to the optical redshift of the Coma cluster, and the dotted and dash-dotted lines show the redshift of ± 1000 and ± 2000 km, respectively.

error. Because $\sigma_k^{(\mathrm{XIS}\text{-}i)}$ was ignored in these estimates, the obtained value is an upper limit for intrachip variation within a 68% confidence level.

In summary, the intrachip variation is an upper limit, and is larger than the gain uncertainty. Thus, we concluded from (i) and (ii) that the $1\,\sigma$ systematic error within a 68% confidence level is 11 eV. The systematic error is then 18 eV, which corresponds to 818 km s^{-1} in the line of sight velocity, when we quote the 90% confidence level.

4.5.2. Redshift measurements from two different spectral models

As mentioned in subsections 3.2 and 3.3, the line-of-sight velocity of the ICM or redshift can be evaluated using two different spectral models: the APEC model or the bremsstrahlung with three Gaussian lines. It is then useful to compare these results, and to see if there is any systematic uncertainty in the redshift measurement due to spectral modeling. In the APEC model, the temperature dependence of the Fe Kα line energy is already implemented in the plasma code, which in turn evokes a parameter coupling between the temperature and the line energy (or redshift). On the other hand, in the bremsstrahlung + Gaussians model, the line centroid should be determined almost independently of the continuum temperature, although its temperature dependence has to be corrected later. We made this correction by deriving the rest-frame Fe Kα centroid energy as a function of temperature on the basis of spectral simulations, assuming the APEC model and XIS energy responses.

In figure 12 left, a comparison of redshift measured by the two different models is shown for all analysis regions defined in figure 1. Because there is consistency between the two within their statistical errors, we conclude that either method robustly determines the ICM redshift for the present observations. Therefore, we will show results of the fits with the APEC model because the uncertainties with APEC are smaller.

4.5.3. Redshift measurement from the APEC model

The obtained redshifts from the spectral fits with the single temperature (APEC) model in the energy range of 5.0–8.0 keV are shown in figure 12 right, where the ICM velocity in the line of sight is also calculated as $v_{\mathrm{l}} \equiv c(z_{\mathrm{obs}} - z_{\mathrm{cl}})$, where z_{obs} is the obtained redshift and z_{cl} is the optical redshift. The resultant redshifts are consistent with the optical redshift in Colless and Dunn (1996) from the NED data base,[2] within the statistical and systematic errors, which corresponds to ± 0.0027 in the redshift. The direct measurements of the central energy of the Kα line of He-like Fe also give almost the same redshifts as those derived from spectral fits with the single-temperature (APEC) model. To quantitatively derive the redshift, we calculated the mean redshift of the ICM in all pointings to be $\langle z_{\mathrm{obs}} \rangle = 0.0227 \pm 0.0005$. This is slightly lower than the optical redshift, $z_{\mathrm{cl}} = 0.0231$, from the NED database, but within 90% error. As can be seen in table 3, in the center and $14'$ offset regions, the derived highest and lowest redshift are $z_{\mathrm{highest}} = 0.0242 \pm 0.001$ for cell numbers 5 and 8 of the center region, and $z_{\mathrm{lowest}} = 0.0209 \pm 0.001$ for cell number 2 of the center region. Based on these redshift measurements, the derived ICM bulk velocities are $v_{\mathrm{highest}} = 330 \pm 300$ km s^{-1}, and $v_{\mathrm{lowest}} = -660 \pm 300$ km s^{-1}. Including systematic errors of ± 818 km s^{-1} with 90% confidence level (sub-subsection 4.5.1), there is no significant difference. We estimated the 90% upper limit on the velocity gradient to be $\Delta v_{\mathrm{l}} = 990 \pm 424 \pm 1157$ km s^{-1}. If we further add systematic and statistical errors in the quadrature, the upper limit of the gas velocity within the 90% confidence level becomes $|\Delta v_{\mathrm{l}}| < 2200$ km s^{-1}. For simplicity, assuming that the gas is rigidly rotating at a typical circular velocity of $\sigma_{\mathrm{r}} \sim |\Delta v_{\mathrm{l}}|/2$, then $\sigma_{\mathrm{r}} = 1100$ km s^{-1}, which does not exceed the sound velocity of the Coma cluster, which is 1500 km s^{-1}

[2] ⟨http://nedwww.ipac.caltech.edu/⟩.

Table 4. Results of the redshift measurement with the single-temperature (APEC) model in the energy range of 5.0–8.0 keV.

Field	X-ray ($z_{\rm obs}$)	Optical ($z_{\rm cl}$)	X-ray ($cz_{\rm obs}$) (km s^{-1})	Optical ($cz_{\rm cl}$) (km s^{-1})
all pointings	0.0227 ± 0.0005	0.02307	6810 ± 150	6917
center	0.0227 ± 0.0005	0.02286	6810 ± 150	6853
14′ offset	0.0230 ± 0.001	0.02286	6900 ± 300	6853
center and 14′ offset	0.0227 ± 0.0005	0.02286	6810 ± 150	6853
NGC 4839	0.0269 ± 0.0033	0.02448	8070 ± 990	7339
center (XIS 0123)	0.0226 ± 0.0005	0.02286	6775 ± 150	6853
center (XIS 012)	0.0226 ± 0.0005	0.02286	6775 ± 150	6853
NGC 4839 (XIS 013)	0.0287 ± 0.0033	0.02448	8604 ± 990	7339
NGC 4839 (XIS 03)	0.0268 ± 0.0033	0.02448	8034 ± 990	7339

* The upper section shows the averaged redshift for each region with all XIS sensors simultaneously. The lower section shows the redshift in each field with the averaged spectral fits. XIS detectors that are included are shown in parentheses. Systematic errors of ± 818 km s^{-1} in X-ray ($cz_{\rm obs}$) were not included in this table. Optical redshifts are referred to Colless and Dunn (1996).

for a temperature of 8 keV. The average redshift in the center region is as follows: 0.0227 ± 0.0011 in the north–west region (cell numbers 8, 9, and 13), 0.0214 ± 0.0013 in the south–west region (cell numbers 10, 11, 14), 0.0236 ± 0.0012 in the north–east region (cell numbers 0, 1, 4, and 5), and 0.0222 ± 0.0012 in the south–east region (cell numbers 2, 3, 6, and 7). We also show the averaged redshift over FOV in the upper panel of table 4. These results are consistent with each other in the center region, and with the observed redshifts in the 14′ offset region within statistical and systematic errors. The difference in the ICM velocity between the center and 30′ offset regions is derived as $\Delta v_{\rm l} = 90 \pm 1350 \pm 818$ km s^{-1}, and the difference between the center and 34′ offset regions is $\Delta v_{\rm l} = -1050 \pm 3300 \pm 818$ km s^{-1}. These are also consistent with each other. Components of the velocity in the plane of the sky were not measured. If we assume that three components are similar, then the limit on the radial velocity translates into a limit of $\sqrt{3} \times 290 \sim 500$ km s^{-1}, which does not exceed the speed of sound, and is consistent with the systematic errors. Therefore, there were no significant velocity variations on the 10′ scale within the central regions (center and 14′, 30′, and 34′ offset regions) from our analysis. In the NGC 4839 subcluster region (44′ offset region), the observed redshift is 0.0269 ± 0.0033, which corresponds to 1140 ± 990 km s^{-1} as the ICM bulk velocity without systematic errors. There also seems to be no significant difference between the core of the Coma cluster and the NGC 4839 subcluster within the 90% confidence level.

As mentioned in sub-subsection 4.5.1, some sensors have large uncertainties in the determination of the line centroid energy. On XIS 3 in the center region, the Mn Kα line centroid energy of segment A was different from others. Similarly, the segment D of XIS 1 in the NGC 4839 region was also different. We averaged the spectrum over FOV in (i) all detectors, and (ii) all detectors except those with different Mn Kα line centroid energies to check the spectral shape and measured redshift in the center and NGC 4839 regions (44′ offset region). The results are shown in the lower section in table 4. For the center region, the derived redshifts were fairly consistent, including XIS 3 or not. On the other hand, for the NGC 4839 subcluster region, the resultant redshift changed slightly from 0.0268 to 0.0287, although this was also consistent within statistical and systematic errors. As shown in figure 11, the peak of the He-like Fe-Kα line of XIS 1 is more shifted than that of the other two sensors. The measured redshifts in the 44′ offset region were 0.0271 ± 0.0023, 0.0303 ± 0.0051, and 0.0255 ± 0.0027 for XIS 0, 1, and 3, respectively. Because the measured redshift of the averaged spectra between XIS 0 and 3 was consistent with the redshift from simultaneous spectral fits, the value 0.0269 would be plausible.

In conclusion, there was no significant difference in the ICM velocity between the core of the Coma cluster and the NGC 4839 subcluster within 90% confidence.

4.6. Fe Abundance of ICM

To measure the abundance using the strong Fe-K lines, we employed the results of spectral fitting in the 5.0–8.0 keV energy range for the Fe abundance. Because of the good statistics, the spectra in the lower energy band primarily determine the fitted temperatures. Although the spectra are well-fitted with a single-temperature model, a small discrepancy between the model and data around the Fe-K line can yield a large systematic uncertainty in the derived Fe abundances. Within the 34′ region, temperatures and abundances derived from the spectral fitting in the 5.0–8.0 keV energy range agree well with those from 1.0–8.0 keV energy ranges within 5%. In the 44′ and 60′ offset regions, the Fe abundances from the 5.0–8.0 keV energy range are smaller than those from the 1.0–8.0 keV range by ~ 0.1 solar. The χ^2 values for the limited energy range of 5.0–8.0 keV from the former fitting are 10% smaller than those from the latter, although the single-temperature model reproduces the observed spectra at 1.0–8.0 keV well. Therefore, we adopted the Fe abundance derived from the spectral fitting in the 5.0–8.0 keV energy range. Figure 13 shows a radial profile and map of the Fe abundance of ICM with the single-temperature (APEC) model in the 5.0–8.0 keV energy range. Within 30′ from the X-ray peak, the Fe abundances are almost constant at ~ 0.4 solar. The derived Fe abundances are 0.41 ± 0.01 solar in the center region, and 0.38 ± 0.02 solar in the 14′ offset region. The Fe abundances in the 30′ and 34′

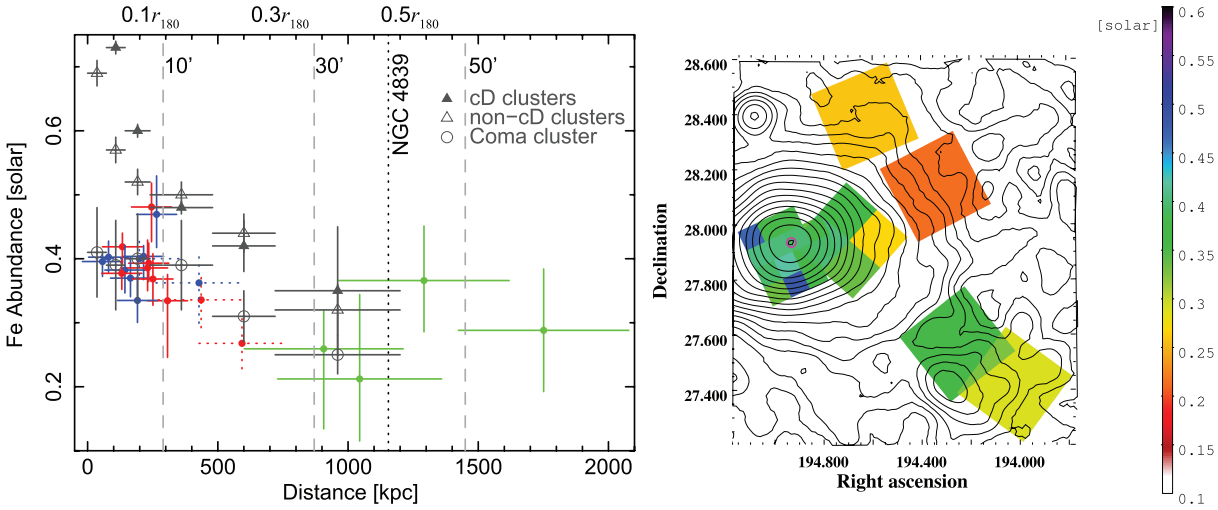

Fig. 13. Left: Radial Fe abundance profile with the single-temperature (APEC) model in the 5.0–8.0 keV energy range measured from the position of the X-ray peak of the Coma cluster. Color and symbol notations are the same as in figure 6. The gray colors show the results from XMM-Newton (Matsushita 2011). Right: Observed Fe abundance map of the Coma cluster in solar units. The magenta circle corresponds to the X-ray peak. The Fe abundance map is overlaid on X-ray contours on a linear scale in the 0.4–2.4 keV energy range with the ROSAT-All-Sky-Survey.

offset regions are slightly lower, ~ 0.3 solar, although it has larger uncertainties. These values agree with recent XMM results (Arnaud et al. 2001; Matsushita 2011) within 1.2 Mpc.

The Fe abundance in the NGC 4839 subcluster region is comparable to that in the central region, and higher than that in the 30′ and 34′ offset regions. The average value in the subcluster region is 0.33 ± 0.09 solar. This value is also consistent with that in Neumann et al. (2001), although the error bars in their results are much larger than those in our results.

5. Discussion

5.1. *Temperature Measurements with Suzaku*

X-ray observations of clusters of galaxies can play a major role in determining cosmological parameters, because of the importance of measuring the gravitational mass. The ratio of He-like Kα to H-like Kα lines of Fe is a very steep function of temperature, and has a different temperature dependence from that of the continuum. The continuum emission is affected by the systematic uncertainties in the response and non-thermal emission, while the line ratio does not. Thus, by comparing the fitted temperatures between these two methods, the effects of the systematic uncertainty in the response and/or of the non-thermal emission is decreased. Using the APEC plasma code, the temperatures derived from the spectral fitting of the 1.0–8.0 keV energy range and the line ratio of Fe agree within a few percent when we averaged all regions. The systematic uncertainties in temperatures from the line ratio are in the level of the systematic difference between those from APEC and MEKAL, which is about 3%. The consistency of observed temperatures from the continuum and those from line ratios supports the accuracy of Suzaku measurements of the plasma temperature. In contrast, systematic differences of $\sim 10\%$ in the cluster temperature among Chandra, PN, and MOS were reported in relatively high-temperature clusters (Snowden et al. 2008). Even using the same instrument, the derived temperatures changed systematically by $\sim 10\%$ between calibrations (Reese et al. 2010; Matsushita 2011).

A systematic uncertainty of several percent in response matrices of a detector can also cause systematic uncertainties in the temperature structure. Matsushita (2011) found that the temperature structures of ICM in the Coma cluster derived from multi-temperature fits with PN and MOS spectra were different, although the two detectors gave consistent temperatures within several percent. When they allowed higher temperature components over 10 keV in hot clusters including the Coma cluster, using MOS data, the Fe abundances from the He-like line increased by several tens of percent, owing to artificial detection of a hot component, while those derived by PN were unchanged. However, with Suzaku, we found that the single-temperature model fits the spectra of the Coma cluster very well, and we do not need temperature components above 10 keV or below 2 keV to fit the spectra. The multi-temperature components observed by XMM were not needed.

In the outer regions of clusters at low surface brightness, uncertainties in the background of Chandra and XMM also lead to systematic uncertainties in the ICM temperatures. Some analyses found that the ICM temperatures decreased outward by half at $0.6\,r_{180}$ (e.g., Vikhlinin et al. 2005; Pratt et al. 2007), while others found flatter profiles (e.g., Arnaud et al. 2005). Systematic uncertainties in the derived temperatures due to uncertainties in the background with Suzaku observations are much smaller, because Suzaku XIS has a much lower and more stable background. Also, previous XMM and Chandra results of temperatures in the outer regions have statistical errors more than 20%, while those of Suzaku have errors less than 10%.

5.2. *Effect on the Search of a Hard Component*

We need precise measurements of the ICM temperatures to search for a non-thermal hard component as an excess of

the thermal component. On the basis of the ICM temperature map derived with XMM-PN, Wik et al. (2009) found that the Suzaku HXD-PIN spectrum was described with the thermal emission from ICM, and there was no significant evidence of excess hard emission. The temperatures of the Coma cluster derived from Suzaku-XIS are consistent within error bars with those from the PN detector: the weighted average of temperatures with statistical errors within the center field is close to that derived with XMM-PN within a few percent. The temperatures of offset fields are consistent with those from XMM-PN within error bars. Thus, our results support the non-detection of non-thermal hard emissions by Wik et al. (2009).

Ota et al. (2008) reported the existence of hot gas at $25.3^{+6.1}_{-4.5}$ keV in RX J1347.5−1145. They concluded that the gas properties can be explained by a fairly recent (within the last 0.5 Gyr) collision of two massive ($5 \times 10^{14}\,M_{\odot}$) clusters with bullet-like high velocity ($\Delta v \sim 4500\,\mathrm{km\,s^{-1}}$). In contrast, Wik et al. (2009) found that there was no extremely high temperature gas in the Coma cluster in the HXD-PIN spectrum up to 70 keV. On the basis of the consistency of the derived temperatures from the continuum and the line ratio and the results from the spectral analysis of HXD-PIN, we conclude that the amount of very high-temperature gas is rather small. From the spatial variation of the derived temperatures, there is no region with extremely hot temperature; the derived temperatures range from 7.0 to 9.0 keV within the center, 14′ offset, and 34′ offset regions.

The Coma cluster has a cluster-wide synchrotron radio halo. If the electrons in the cluster were accelerated by very strong shock that occurred owing to a recent merger, we might expect the cluster to contain more very hot gas, although it is difficult to make this argument quantitative. In any case, in the Coma cluster, relativistic electrons producing the radio halo were apparently generated without producing a large amount of very hot gas. An example of a process that might do this is the turbulent re-acceleration model (e.g., Brunetti et al. 2001).

5.3. Temperature Structure of the Coma Cluster

Within the center and 14′ offset regions, the spatial variation of the derived temperatures is relatively small, from 7 keV to 9 keV. There are no extremely hot and cool regions. We did not detect any temperature jump corresponding to a shock in the offset regions. Within each region for the spectral analysis, the single-temperature model fit the spectrum. Therefore, in the center of the Coma cluster, ICM is in a nearly relaxed state.

Although the variation was small, there was some asymmetric temperature structure, like a hot region northwest of the center. If the cluster had been an isolated system collapsing from self-gravity, the temperature structures would be symmetric. The observed asymmetry in the temperature distribution indicates that external effects or interactions, such as merging, have occurred. Numerical simulations of the evolution of the cluster (e.g., Roettiger et al. 1996; Norman & Bryan 1999) show that nonaxisymmetric structures in the temperature distribution are erased several Gyr after each merger. The presence of asymmetric temperature structures suggest that the central region of the Coma cluster has experienced a merger, and the lack of a hard component shows that its core have relaxed in the last several Gyr.

The observed cool region in the southeast of the center region coincides with the filamentary structure originating near NGC 4911 and NGC 4921 (Vikhlinin et al. 1997; Donnelly et al. 1999). Arnaud et al. (2001) reported that the temperature of this cold area ranges from 5 to 7 keV. This region mostly contains the stripped subcluster gas, which is thought to be relatively cool in the initial state. Numerical simulations (e.g., Schindler & Müller 1993) suggest that the gas would maintain its temperature for several Gyr. Ishizaka and Mineshige (1996) showed that even a single subcluster collision with supersonic velocity creates both hot and cool regions in the main cluster. Although heating due to collisions occurs, cooling would also occur through the adiabatic expansion of the stripped gas.

5.4. Searching for Gas Bulk Motions

The measurements of bulk motions in ICM are also important to derive the gravitational mass of clusters of galaxies. We constrained the upper limit of ICM bulk motions in the center and 14′ offset regions on the scale of 130 kpc (4.′5) and 260 kpc (9′), respectively, which correspond to the scales of regions for spectral accumulation (see section 2 and sub-subsection 4.5.3). The upper limit of gas bulk motions is $|\Delta v_{\mathrm{l}}| < 1100\,\mathrm{km\,s^{-1}}$. As summarized in table 4, considering the systematic error of 18 eV, or $818\,\mathrm{km\,s^{-1}}$ with a 90% confidence level (sub-subsection 4.5.1), there are no significant bulk motions in the center and 14′ offset fields. Compared with the sound velocity of the Coma cluster, $s = [\gamma kT/(\mu m_{\mathrm{p}})]^{1/2} \sim 1500\,\mathrm{km\,s^{-1}}$ for a temperature of $kT = 8$ keV, the bulk-motion in the central region of the Coma cluster does not exceed the sound velocity.

Our results do not conflict with the discovery of pressure fluctuations in the center of the Coma cluster by Schuecker et al. (2004), which indicates that at least 10% of the ICM pressure is in turbulent form. We have not constrained the turbulence, and the scale of the fluctuation ranges between 29 kpc and 64 kpc, which is smaller than our scale of spectral analysis.

The velocity difference between the main cluster and the NGC 4839 subcluster from optical observations is $486\,\mathrm{km\,s^{-1}}$. Although the best-fit line-of-sight velocity of the subcluster is higher than that of the main cluster by $\sim 1000\,\mathrm{km\,s^{-1}}$, the difference is comparable to statistical and systematic errors. Because the temperature of the region is about 5 keV, the sound velocity is $\sim 1150\,\mathrm{km\,s^{-1}}$. Considering the error bars, we conclude that the relative line-of-sight gas velocity in the NGC 4839 subgroup region does not greatly exceed the sound velocity.

Numerical simulations indicate that a major merger between clusters raises the temperature of ICM and induces a bulk velocity of the order of $1000\,\mathrm{km\,s^{-1}}$ (e.g., Roettiger et al. 1996; Norman & Bryan 1999). In the late phase of mergers, turbulent motions develop in a simulation by Takizawa (2005). The non-detection of bulk-motions in ICM of the Coma cluster also indicates that the central region of the cluster is in a somewhat relaxed state. If so, the non-thermal electrons relevant to the radio halo of the Coma cluster may have been accelerated by the intracluster turbulence rather than shocks. In conclusion, the line-of-sight gas velocity of the Coma cluster in the observed region does not greatly exceed the sound velocity, and the central region of the Coma cluster is in a nearly relaxed

state. This means that the assumption of hydrostatic equilibrium is approximately valid in calculating the cluster mass of the Coma cluster.

5.5. *Fe Abundance Map*

The Fe abundance is nearly constant at ~ 0.4 solar within a clustocentric radius of 0.5 Mpc, and beyond that distance it decreases with the radius to 0.2–0.3 solar. This profile is consistent with those measured by XMM (Arnaud et al. 2001; Matsushita 2011). Suzaku has a lower level of background, and a slightly better energy resolution; therefore, systematic uncertainties in Fe abundance are considered to be smaller.

Differences in abundance profiles of ICM in central regions of clusters with and without cool cores have been reported (Fukazawa et al. 2000; de Grandi & Molendi 2001; Matsushita 2011). Matsushita (2011) showed an abundance difference between the two type of clusters within $0.1\,r_{180}$, while at 0.1–$0.3\,r_{180}$, the average values of Fe abundances are both ~ 0.4–0.5 solar, and are consistent with each other.

The Coma cluster is thought to have experienced a major merger in the recent past and, subsequently, the central region came to a somewhat relaxed state. During a cluster merger, the mixing of ICM could destroy any central Fe peak. In the first stage of merging, the Fe peak and cool core remain intact as observed in some ongoing merging clusters (Molendi et al. 2000; Sun et al. 2002). For example, Abell 2256, an ongoing merging cluster, has an abundance gradient in the direction opposite of the merging direction owing to the remixing of the gas. Numerical simulations also support this scenario. Schindler et al. (2005) performed hydrodynamical simulations with two different merger types of clusters: Cluster 1 has only small merger events, while Cluster 2 undergoes a major merger (mass ratio 1:3). In Cluster 1, the abundance is more than ~ 0.4 solar within a radius of 0.1 Mpc, and decreases from ~ 0.3 solar to ~ 0.1 solar with a decrease in radius. The situation is different in Cluster 2. In the Coma cluster, the Fe abundance is ~ 0.4 solar and homogeneous within a radius of 0.5 Mpc. This value of the Fe abundance is similar to those at 0.2–$0.3\,r_{180}$ in other clusters, as shown in figure 13. Therefore, in the Coma cluster, the merger have destroyed the cool core, and mixed the ICM completely, at least within 0.5 Mpc.

6. Summary and Conclusion

The Coma cluster, which was observed with the X-ray Imaging Spectrometer (XIS) onboard Suzaku, was analyzed by the X-ray satellite in six pointings, centered on the X-ray peak and offset by $14'$ west, $30'$, $34'$, $44'$, and $60'$. Because of its low background, Suzaku is the most sensitive X-ray satellite for observing Kα lines of Fe in the ICM. After obtaining accurate measurements of Fe lines, we studied the temperature structure of the ICM, searched for possible bulk-motions, and measured the Fe abundance in the cluster.

The spectra of each extracted region were well fitted by the single-temperature APEC model, and the two- or three-temperature APEC model did not improve χ^2. The temperatures derived from the observed ratios of Kα lines of H-like and He-like Fe agree well with those from spectral fittings with the single-temperature APEC model. Because this line ratio is a strong function of plasma temperature, the observed consistency supports the accuracy of temperature measurements with Suzaku, and constrains the temperature structure of the ICM.

The observed values of the central energy of the He-like Fe line of the center, $14'$, $30'$, and $34'$ offset regions are constant within $500\,\mathrm{km\,s^{-1}}$, which corresponds to the calibration error. Because the relative bulk velocities in the Coma cluster are smaller than the sound velocity of the ICM, $1500\,\mathrm{km\,s^{-1}}$, we can verify the derived total mass in a cluster on the basis of the hydrostatic ICM equilibrium inside the $34'$ offset region. Significant bulk velocities were also not found in the $44'$ offset region, which corresponds to the NGC 4839 subcluster.

The results on the temperature and velocity structure suggest that the core of the Coma cluster is in a fairly relaxed state. This is consistent with models in which the non-thermal electrons relevant to the radio halo are accelerated by the intracluster turbulence rather than large-scale shocks. This is also consistent with the fact that numerical simulations show that the turbulence motion is developed in the late phase of mergers.

The observed Fe abundance of the ICM is almost constant at 0.4 solar inside the $34'$ offset region, and decreases with the radius. The central abundance is slightly lower than that of other clusters or groups. This indicates that the central regions of the gas were mixed well during the past merger growth of the cluster.

We wish to thank the referee for his/her suggestions on the paper. The authors are grateful to all members of Suzaku for their contributions in instrument preparation, spacecraft operation, software development, and in-orbit instrumental calibration. To analyze the data, we used the ISAS Analysis Servers provided by ISAS/C-SODA. N. O. acknowledges support by the Ministry of Education, Culture, Sports, Science and Technology of Japan, Grant-in-Aid for Scientific Research No. 22740124. C. L. S. was supported in part by NASA Suzaku grants NNX08AZ99G, NNX09AH25G, and NNX09AH74G.

References

Arnaud, M., et al. 2001, A&A, 365, L67
Arnaud, M., Pointecouteau, E., & Pratt, G. W. 2005, A&A, 441, 893A
Biviano, A., 1998, in Untangling Coma Berenices: A New Vision of an Old Cluster, ed. A. Mazure et al. (Singapore: World Scientific), 1
Briel, U. G., Henry, J. P., & Böhringer, H. 1992, A&A, 259, L31
Brown, S., & Rudnick, L. 2011, MNRAS, 412, 2
Brunetti, G., Setti, G., Feretti, L., & Giovannini, G. 2001, MNRAS, 320, 365
Buote, D. A. 2001, ApJ, 553, L15
Burns, J. O., Roettiger, K., Ledlow, M., & Klypin, A. 1994, ApJ, 427, L87

Colless, M., & Dunn, A. M. 1996, ApJ, 458, 435
de Grandi, S., & Molendi, S. 2001, ApJ, 551, 153
Donnelly, R. H., Markevitch, M., Forman, W., Jones, C., Churazov, E., & Gilfanov, M. 1999, ApJ, 513, 690
Dupke, R. A., & Bregman, J. N. 2001, ApJ, 562, 266
Dupke, R. A., & Bregman, J. N. 2006, ApJ, 639, 781
Eckert, D., Neronov, A., Courvoisier, T. J.-L., & Produit, N. 2007 A&A, 470, 835
Feretti, L., & Giovannini, G. 1998, in A new view of an Old Cluster: Untangling Coma Berenices, ed. A. Mazure et al. (Singapore: World Scientific), 123
Fitchett, M., & Webster, R. 1987, ApJ, 317, 653
Fujita, Y., et al. 2008, PASJ, 60, 1133
Fukazawa, Y., Makishima, K., Tamura, T., Nakazawa, K., Ezawa, H., Ikebe, Y., Kikuchi, K., & Ohashi, T. 2000, MNRAS, 313, 21
Fusco-Femiano, R., dal Fiume, D., Feretti, L., Giovannini, G., Grandi, P., Matt, G., Molendi, S., & Santangelo, A. 1999, ApJ, 513, L21
Fusco-Femiano, R., Landi, R., & Orlandini, M. 2007, ApJ, 654, L9
Fusco-Femiano, R., Orlandini, M., Brunetti, G., Feretti, L., Giovannini, G., Grandi, P., & Setti, G. 2004, ApJ, 602, L73
Hattori, M., Kneib, J.-P., & Makino, N. 1999, Prog. Theor. Phys. Suppl., 133, 1
Honda, H., et al. 1996, ApJ, 473, L71
Ishisaki, Y., et al. 2007, PASJ, 59, 113
Ishizaka, C., & Mineshige, S. 1996, PASJ, 48, L37
Kalberla, P. M. W., Burton, W. B., Hartmann, D., Arnal, E. M., Bajaja, E., Morras, R., & Pöppel, W. G. L. 2005, A&A, 440, 775
Koyama, K., et al. 2007, PASJ, 59, S23
Kushino, A., Ishisaki, Y., Morita, U., Yamasaki, N. Y., Ishida, M., Ohashi, T., & Ueda, Y. 2002, PASJ, 54, 327
Liedahl, D. A., Osterheld, A. L., & Goldstein, W. H. 1995, ApJ, 438, L115
Lodders, K. 2003, ApJ, 591, 1220
Lumb, D. H., Warwick, R. S., Page, M., & De Luca, A. 2002, A&A, 389, 93
Lutovinov, A. A., Vikhlinin, A., Churazov, E. M., Revnivtsev, M. G., & Sunyaev, R. A. 2008, ApJ, 687, 968
Matsushita, K. 2011, A&A, 527, A134
Mellier, Y., Mathez, G., Mazure, A., Chauvineau, B., & Proust, D. 1988, A&A, 199, 67
Merritt, D., & Trimbley, B. 1994, AJ, 108, 514
Mewe, R., Gronenschild, E. H. B. M., & van den Oord, G. H. J. 1985, A&AS, 62, 197
Mewe, R., Lemen, J. R., & van den Oord, G. H. J. 1986, A&AS, 65, 511
Mitsuda, K., et al. 2007, PASJ, 59, S1
Molendi, S., de Grandi, S., & Fusco-Femiano, R. 2000, ApJ, 533, L43
Neumann, D. M., et al. 2001, A&A, 365, L74
Norman, M., L., & Bryan, G. L. 1999, The Radio Galaxy Messier 87, ed. H.-J. Röser & K. Meisenheimer (Berlin: Springer), 106
Ota, N., et al. 2007, PASJ, 59, S351
Ota, N., et al. 2008, A&A, 491, 363
Ota, N., Pointecouteau, E., Hattori, M., & Mitsuda, K. 2004, ApJ, 601, 120
Pratt, G. W., Böhringer, H., Croston, J. H., Arnaud, M., Borgani, S., Finoguenov, A., & Temple, R. F. 2007, A&A, 461, 71
Reese, E. D., Kawahara, H., Kitayama, T., Ota, N., Sasaki, S., & Suto, Y. 2010, ApJ, 721, 653
Renaud, M., Bélanger, G., Paul, J., Lebrun, F., & Terrier, R. 2006, A&A, 453, L5
Rephaeli, Y., & Gruber, D. 2002, ApJ, 579, 587
Roettiger, K., Burns, J. O., & Locken, C. 1996, ApJ, 473, 651
Rosetti, M., & Molendi, S. 2004, A&A, 414, L41
Sanders, J. S., Fabian, A. C., & Smith, R. K. 2011, MNRAS, 410, 1797
Sato, K., Matsushita, K., Ishisaki, Y., Yamasaki, N. Y., Ishida, M., Sasaki, S., & Ohashi, T. 2008, PASJ, 60, S333
Schindler, S., et al. 2005, A&A, 435, L25
Schindler, S., & Müller, E. 1993, A&A, 272, 137
Schuecker, P., Böhringer, H., Reiprich, T. H., & Feretti, L. 2001, A&A, 378, 408
Schuecker, P., Finoguenov, A., Miniati, F., Böhringer, H., & Briel, U. G. 2004, A&A, 426, 387
Smith, R. K., Brickhouse, N. S., Liedahl, D. A., & Raymond, J. C. 2001, ApJ, 556, L91
Snowden, S. L., Mushotzky, R. F., Kuntz, K. D., & Davis, D. S. 2008, A&A, 478, 615
Sugawara, C., Takizawa, M., & Nakazawa, K. 2009, PASJ, 61, 1293
Sun, M., Murray, S. S., Markevitch, M., & Vikhlinin, A. 2002, ApJ, 565, 867
Takahashi, T., et al. 2007, PASJ, 59, S35
Takei, Y., et al. 2008, ApJ, 680, 1049
Takizawa, M. 2005, ApJ, 629, 791
Tamura, T., Hayashida, K., Ueda, S., & Nagai, M. 2011, PASJ, 63, S1009
Tawa, N., et al. 2008, PASJ, 60, S11
Vikhlinin, A., Forman, W., & Jones, C. 1997, ApJ, 474, L7
Vikhlinin, A., Markevitch, M., Murray, S. S., Jones, C., Forman, W., & Van Speybroeck, L. 2005, ApJ, 628, 655
Watanabe, M., Yamashita, K., Furuzawa, A., Kunieda, H., & Tawara, Y. 1999, ApJ, 527, 80
White, S. D. M., Briel, U. G., & Henry, J. P. 1993, MNRAS, 261, L8
Wik, D. R., Sarazin, C. L., Finoguenov, A., Matsushita, K., Nakazawa, K., & Clarke, T. E. 2009, ApJ, 696, 1700
Yoshino, T., et al. 2009, PASJ, 61, 805